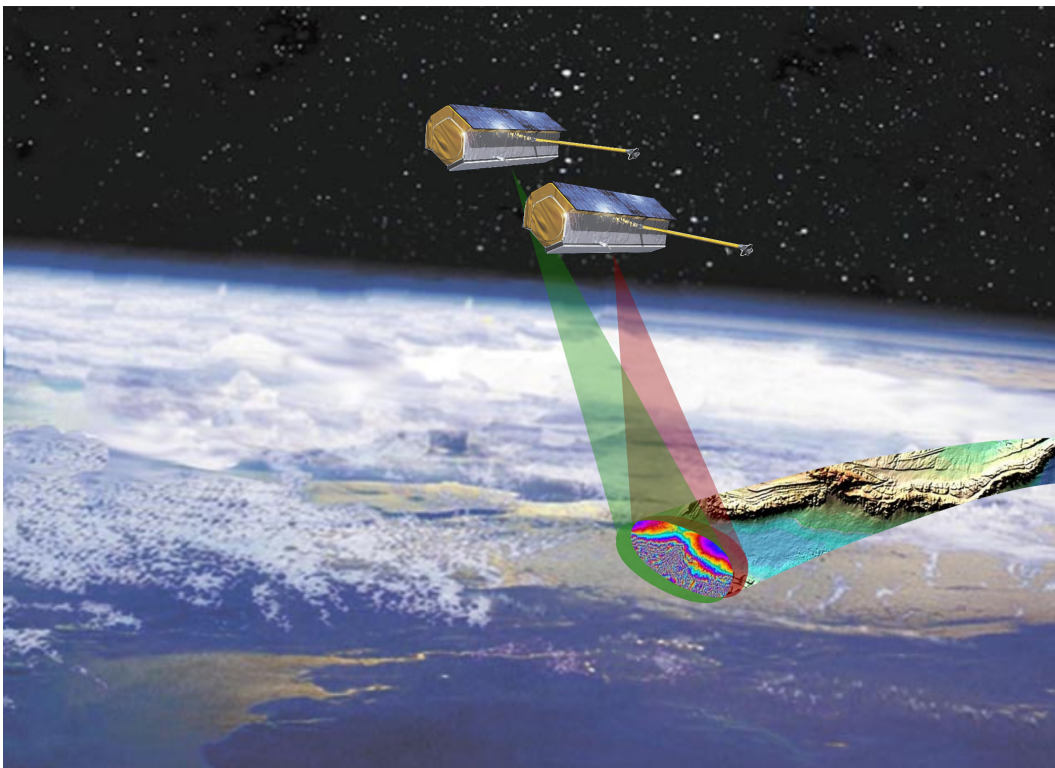


Satellite Formation Flying for High-Precision Earth Observation

Pol Francesch Huc, Sydney Hsu



AA 279D - Spacecraft Formation-Flying and Rendezvous
Stanford University

Revision History

Table 1: Summary of project revisions.

Rev	Changes
PS1	- Created document - Added problem set 1 material
PS2	- Added problem set 2 material - Revised PS1 orbital elements and updated document accordingly

Contents

0	Scope	5
1	Problem Set 1	5
1.1	Problem 1: Your Mission, Your Challenge	5
1.1.a	Reference Mission	5
1.1.b	Mission Objectives	5
1.1.c	Spacecraft Specification	6
1.1.d	Launch and Orbit	6
1.1.e	Synthetic Aperture Radar Payload	7
1.1.f	Key Dynamics, Guidance, Navigation & Control Requirements	8
1.2	Problem 2: Orbit Simulation, Review of Astrodynamics	8
1.2.a	Initial Orbital Elements	8
1.2.b	Initial Position and Velocity	9
1.2.c	Unperturbed and J2 Propagation Numerical Simulations	10
1.2.d	Unperturbed Numerical and Analytical Comparison	10
1.2.e	Osculating Orbital Elements from Numerical Simulation	12
1.2.f	Mean Classical Orbital Elements	14
1.2.g	Reconciling Osculating and Mean Orbital Elements	16
2	Problem Set 2	17
2.1	Problem 1: Everything is Relative	17
2.1.a	Chief and Deputy Orbit Initialization	17
2.1.b	Numerical Integration of Relative Equations of Motion	17
2.1.c	Analytical Solution to Fundamental Orbital Differential Equations	20
2.1.d	Numerical and Analytical Comparison	21
2.1.e	Drift Correction Maneuver	24
2.1.f	Maneuver Simulation	24
3	References	26
4	Appendix A: Code	27

List of Figures

1	TerraSAR-X spacecraft features. [3]	6
2	Helix satellite formation of TerraSAR-X and TanDEM-X illustrating relative orbits (left) and cross-track baselines as a function of orbit position (right). [2]	7
3	Data acquisition modes: Monostatic (left), bistatic (middle), and alternating bistatic (right). [2]	8
4	Simulated TDS orbital path starting on 15 June 2007 (1000 orbits).	10
5	Absolute position and velocity errors of the numerical integration with respect to the analytical solution in the RTN frame.	12
6	Orbital elements, specific angular momentum, and specific energy over 5 orbits for J2 (blue) and unperturbed (red) propagation.	13
7	Line of apsides and specific angular momentum over 5 orbits for J2 (blue) and unperturbed (red) propagation.	14
8	Orbital elements, specific angular momentum, and specific energy over 5 orbits for J2 (blue), unperturbed (red), and mean classical (yellow) orbit propagation.	15
9	Line of apsides and specific angular momentum over 5 orbits for J2 (blue), unperturbed (red), and mean classical (yellow) orbit propagation.	15
10	Isolating seemingly unperturbed parameters of the mean classical orbit propagation reveals small precession.	16
11	Numerically integrated relative RTN position of the deputy (TDX) with respect to the chief (TSX) using the non-linear equations of relative motion.	18
12	Numerically integrated relative RTN velocity using the non-linear equations of relative motion.	19
13	Overlaid numerically integrated (blue) and analytically determined (red) relative RTN position.	20
14	Overlaid numerically integrated (blue) and analytically determined (red) relative RTN velocity.	21
15	Position error in the RTN frame between the numerical and analytical solutions.	22
16	Velocity error in the RTN frame between the numerical and analytical solutions.	22
17	Position error between the numerical and analytical solutions with a difference in initial semi-major axis.	23
18	Numerically integrated relative RTN position with a difference in initial semi-major axis.	23
19	Numerically integrated relative RTN position before (blue) and after (red) the maneuver.	25
20	Numerically integrated relative RTN velocity before (blue) and after (red) the maneuver.	25

List of Tables

1	Summary of project revisions.	1
2	Comparison of DTED-2 and HRTE-3 specifications [2]	5
3	Initial orbital parameters of TSX and TDX in Helix formation.	17

0 Scope

This report introduces the project, mission specifications, and orbit simulations for AA279D Dynamics, Navigation and Control of Distributed Space Systems.

1 Problem Set 1

1.1 Problem 1: Your Mission, Your Challenge

1.1.a Reference Mission

This project is based on TanDEM-X, a formation-flying satellite mission performing Earth observation using interferometric Synthetic Aperture Radar (SAR) to create a Digital Elevation Model (DEM). The TanDEM-X satellite was launched as an extension joining its twin, TerraSAR-X and both satellites are operated by the German Aerospace Center (DLR). Data is managed and distributed by the European Space Agency (ESA), and the satellites were built by Airbus Defense and Space [1].

1.1.b Mission Objectives

The primary goal of the mission is to create high-precision 3-dimensional models of the Earth's surface to the High-Resolution Terrain Elevation Level 3 (HRTE-3) model specification as defined by the National Geospatial Agency. Images produced by the SAR instruments aid monitoring of land and coastal processes including vegetation, glacial melt, and ocean currents. With the capability of collecting global data across the poles, this mission is critical for a range of science, government, military, and commercial applications. The secondary objective of TanDEM-X is to demonstrate novel SAR techniques in flight (including digital beamforming, along-track interferometry with a varying baseline, and super-resolution). This mission demonstrates a new orbit concept allowing for safe formation flying at close proximity between the two spacecraft [1].

Prior to TanDEM-X, DEMs have lacked full global coverage and precision required for modern navigation, military operations, and scientific applications [2]. As shown in Table 2, the novel DEM standard generated by TanDEM-X (HRTI-3) compared to the previous state-of-the-art (DTED-2) is significantly more accurate across the board, and provides spatial resolution that is sharper by more than a factor of 2.

Table 2: Comparison of DTED-2 and HRTE-3 specifications [2]

Requirement	Specification	DTED-2	HRTI-3
Relative Vertical Accuracy	90% linear point-to-point error over a $1^\circ \times 1^\circ$ cell	12 m (slope < 20%) 15 m (slope > 20%)	2 m (slope < 20%) 4 m (slope > 20%)
Absolute Vertical Accuracy	90% linear error	18 m	10 m
Relative Horizontal Accuracy	90% circular error	15 m	3 m
Horizontal Accuracy	90% circular error	23 m	10 m
Spatial Resolution	independent pixels	30 m (1 arc sec @ equator)	12 m (0.4 arc sec @ equator)

1.1.c Spacecraft Specification

The mission relies on formation flying involving the TanDEM-X (TDX) and TerraSAR-X (TSX) satellites. The two satellites are nearly identical and are equipped with identical X-band SAR instruments to collect high-resolution Earth images as shown by Figure 1. The main difference is that TanDEM-X features an inter-satellite S-band receiver which it uses to receive status and GPS information from TerraSAR-X. It also has been upgraded with an advanced cold-gas propulsion system for fine formation-keeping maneuvers [1] [2].

TerraSAR-X has a wet mass of 1230 kg (of which 78 kg are propellant) and have dimensions of 5m x 2.4 m. While TanDEM-X has the same dimensions, it is heavier at 1340 wet mass (of which 120 kg are propellant). The SAR antennae have dimensions of 5 m x 0.8 m and the average spacecraft power is 800 W [1] [3].

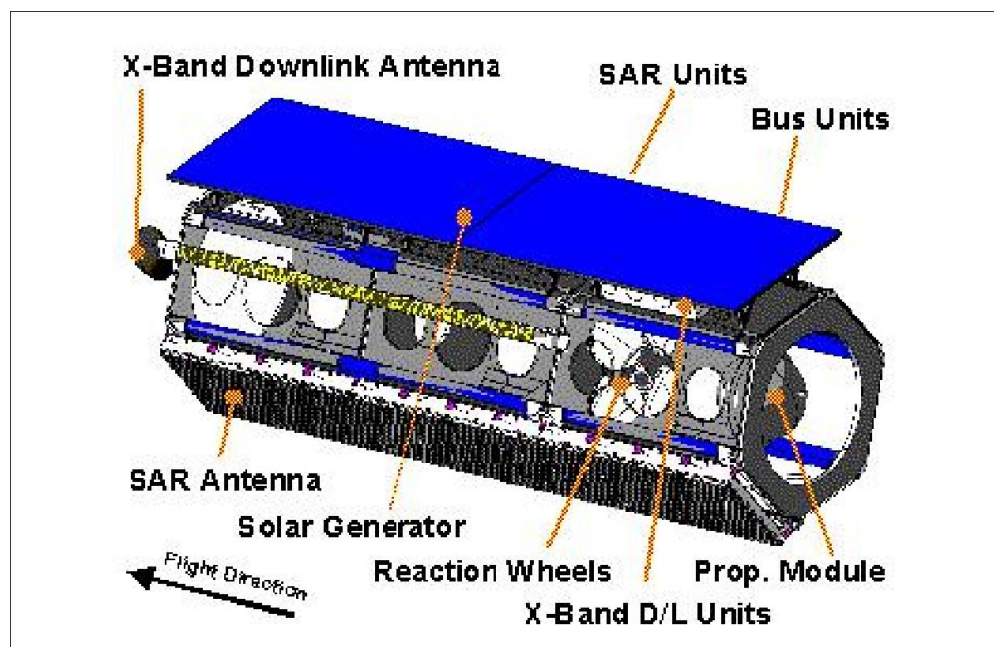


Figure 1: TerraSAR-X spacecraft features. [3]

1.1.d Launch and Orbit

TerraSAR-X remains in the sun-synchronous dawn-dusk circular orbit at which it was launched. Its orbit is described by a mean altitude of 514.8 km (between 505-533 km), an inclination of 97.44° and a local equator crossing time of 18:00 on the ascending node with a nominal revisit period of 11 days (and 167 orbits in the repeat) [1] [3]. The satellite was launched on June 15, 2007 from Baikonur Cosmodrome, Kazakhstan. The mission was designed for 5 years with a goal of a 6.5-year design life. As of January 2022, TerraSAR-X is still performing scientific operations in space [1].

The TanDEM-X spacecraft was launched in June 21, 2010 from Baikonur. Given the close formation with TerraSAR-X as required by the SAR mission, it is of no surprise that TanDEM-X has a practically identical orbit. To set up an effective baseline, TanDEM-X is separated in the right ascension of the ascending node with a small offset in eccentricity. A horizontal baseline between the two spacecraft is

maintained between 200 and 3000 m, depending on DEM generation requirements at different latitudes.

The relative orbits of the two spacecraft is known as a Helix formation, which allows for relatively small distances between the satellites throughout the absolute orbits while minimizing risk of collision at the poles as depicted in Figure 2. This is achieved by combining out-of-plane displacement through different ascending nodes (e.g. $\Delta\Omega = \{300m, 400m, 500m\}$) and radial separation through different eccentricity vectors (e.g. $\Delta e = \{300m, 500m\}$). In the Helix formation, there are no crossings between the two orbits, so arbitrary along-track shifts in the orbits can be performed to finely adjust the baseline [1]. The implication of this formation is that maximum radial separation is achieved at the poles and maximum normal separation at the equator.

TanDEM-X was designed with a mission life of 5 years, and as of January 2022 is still providing SAR imagery after 12 years in orbit [1]. Both TanDEM-X and TerraSAR-X are loaded with enough fuel to continue their mission until 2026 [1].

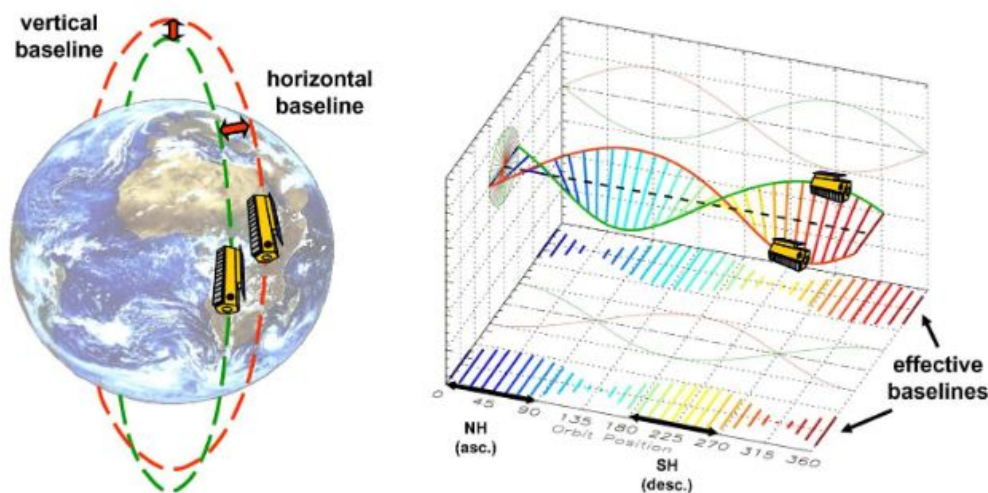


Figure 2: Helix satellite formation of TerraSAR-X and TanDEM-X illustrating relative orbits (left) and cross-track baselines as a function of orbit position (right). [2]

1.1.e Synthetic Aperture Radar Payload

The scientific basis of this mission is Synthetic Aperture Radar (SAR), a method of active remote sensing operable during the day, at night, and even through cloud coverage. The technology works by broadcasting a radar signal to the Earth and picking up the reflections. Comparing the reflected signal with the broadcast reveals the nature of the reflector, whether land, water, snow, ice, or otherwise [4]. In the case of TerraSAR-X and TanDEM-X, interferometric SAR can be conducted in four configurations: bistatic, monostatic, alternating bistatic, and simultaneous transmit as described in [2]. A visualization of three of these modes is shown in Figure 3.

- *Bistatic*: This mode is used to generate the DEM. One of the satellites acts as a transmitter over a common radar footprint. Both satellites collect the reflected signals and comparison of the difference generates the DEM.
- *Monostatic*: This mode has the satellites acting independently, allowing operators to skip the difficult synchronization process. With a relatively long baseline (~ 10 km), this mode is meant as a

backup in case synchronization is not feasible and generates a lower accuracy DEM.

- *Alternating bistatic*: This is similar to the bistatic mode, except that the transmitter is switched at every pulse. This mode is used to calibrate the bistatic SAR interferometer.
- *Simultaneous transmit*: In this mode, both spacecraft transmit at the same time, but the spacecraft maintain a close baseline. This mode allows for accurate synchronization and further calibration of the SAR instrument at the cost of lower range resolution for each individual image.

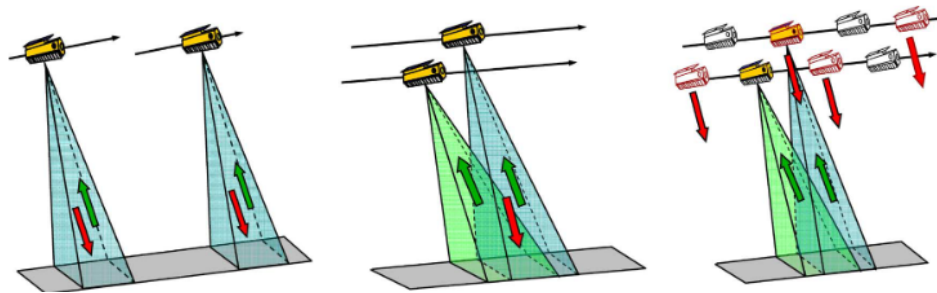


Figure 3: Data acquisition modes: Monostatic (left), bistatic (middle), and alternating bistatic (right). [2]

1.1.f Key Dynamics, Guidance, Navigation & Control Requirements

For SAR data collection, close-proximity formation-flying while maintaining relative separation is mission-critical. To conduct bistatic interferometry, the satellites must be maintained within a tube 250 m in radius for the duration of the mission [1]. Separation in eccentricity and ascending node is also critical to keep the two satellites in Helix formation and to maximize safety. Radial and normal separation shall not be simultaneously zero to avoid collision.

Furthermore, certain SAR techniques require tight formation-keeping and localization. Station-keeping thrusters on TanDEM-X regularly fire to counteract drift associated with J2 perturbation. At specific locations of interest, osculating along-track separations must be sufficiently precise to perform along-track interferometry.

Both spacecraft employ GPS, with TerraSAR-X demonstrating an absolute navigational accuracy of 5 cm [1]. The relative baseline between them, which is typically between 500 and 1500 km, has a 1-mm accuracy requirement in order to achieve high-precision DEM [1]. Relative control accuracy requirements are 28 m in cross-track and 200 m in along-track directions, which TanDEM-X has significantly surpassed with nominal accuracies of 5 m in cross-track and 30 m in along-track [1].

1.2 Problem 2: Orbit Simulation, Review of Astrodynamics

1.2.a Initial Orbital Elements

Given the close formation of the two spacecraft, the initial conditions are chosen to be the same orbit for the purposes of this exercise. We pick the initial conditions from TSX, which was launched on June 15, 2007 into a sun-synchronous orbit with a mean altitude of 514.8 km and inclination of 97.44° . This orbit has a local equator crossing time of 18:00 on the ascending node and was launched on the summer solstice,

corresponding to a right ascension of the ascending node (RAAN) of $\Omega = 270^\circ$. The nominal revisit period is 11 days (and 167 orbits in the repeat). The orbit is circular, corresponding to an eccentricity $e = 0$. The initial conditions can be described using the classical Keplerian orbital elements semimajor axis a , inclination i , eccentricity e , argument of periapsis ω , RAAN Ω , and true anomaly f :

$$\begin{aligned} a &= 6892.927 \text{ km} & \omega &= 0^\circ \\ i &= 97.44^\circ & \Omega &= 270^\circ \\ e &= 0 & f &= 0^\circ \end{aligned}$$

The argument of periapsis, and the true anomaly are not well defined for circular inclined orbits though. Additionally, having eccentricity equal to 0 can create numerical instability in code (and orbits are never perfectly circular anyways). Because of these reasons, we choose to model the following set of orbital elements instead of the classical set:

$$\begin{aligned} a &= 6892.927 \text{ km} & i &= 97.44^\circ \\ \Omega &= 270^\circ & u &= 0^\circ \\ e_x &= 1 \times 10^{-4} & e_y &= 1 \times 10^{-4} \end{aligned}$$

Note that we have chosen the argument of latitude $u = \omega + f$ and the components of the eccentricity vector $e = \sqrt{e_x^2 + e_y^2}$ to replace ω, f, e . Additionally, since the location of the periapsis is undefined for circular orbits such as this one, we propose that the behaviour of the argument of latitude is similar to the true anomaly, since we can set the argument of periapsis to be arbitrarily 0, and get $u = f$.

1.2.b Initial Position and Velocity

As this is an Earth-centered satellite mission, the inertial reference frame of choice will be Earth Centered Inertial (ECI). The initial Keplerian orbital elements are converted to position and velocity in the ECI frame by first expressing them in the perifocal frame and then performing three coordinate rotations (3-1-3 Euler sequence) about each axis by the right ascension of the ascending node, inclination, and argument of periapsis. In the perifocal frame, position and velocity are given by:

$${}^P\vec{r} = \frac{a(1 - e^2)}{1 + e \cos u} \begin{bmatrix} \cos u \\ \sin u \\ 0 \end{bmatrix} \quad (1)$$

$${}^P\vec{v} = \sqrt{\frac{\mu}{a(1 - e^2)}} \begin{bmatrix} -\sin u \\ e + \cos u \\ 0 \end{bmatrix} \quad (2)$$

The transformation matrix from the perifocal to the ECI frame is given by the following, where $R_k(\theta)$ represents the direction cosine matrix rotating about the k -axis by an angle θ :

$$R_{PQW}^{ECI} = R_z(-\Omega)R_x(-i) \quad (3)$$

From these equations, the initial position and velocity in the ECI frame is found to be:

$$\begin{aligned} {}^I\vec{r}_{0,ECI} &= [0 \quad -6892.9 \quad 0] \text{ km} \\ {}^I\vec{v}_{0,ECI} &= [-0.9847 \quad 0 \quad 7.5404] \text{ km/s} \end{aligned}$$

1.2.c Unperturbed and J2 Propagation Numerical Simulations

The orbit tracks shown in Figure 4 show a circular orbit under unperturbed and perturbed propagation. Introducing J2 perturbations causes a nodal precession of the orbit due to the non-spherical mass distribution of the Earth. The J2 acceleration is expressed in ECI by [5]:

$${}^{ECI}a_{J2} = \frac{3J_2\mu R_E^2}{2||\vec{r}||^5} \left[\left(5\frac{r_k^2}{||\vec{r}||^2} - 1 \right) (r_i\hat{I} + r_j\hat{J}) + \left(5\frac{r_k^2}{||\vec{r}||^2} - 3 \right) r_k\hat{K} \right] \quad (4)$$

This was applied as a disturbing force \vec{d} to the 2-body differential equations of motion, which was subsequently solved by numerical integration using MATLAB *ode45*.

$$\ddot{\vec{r}} + \frac{\mu\vec{r}}{r^3} = \vec{d} \quad (5)$$

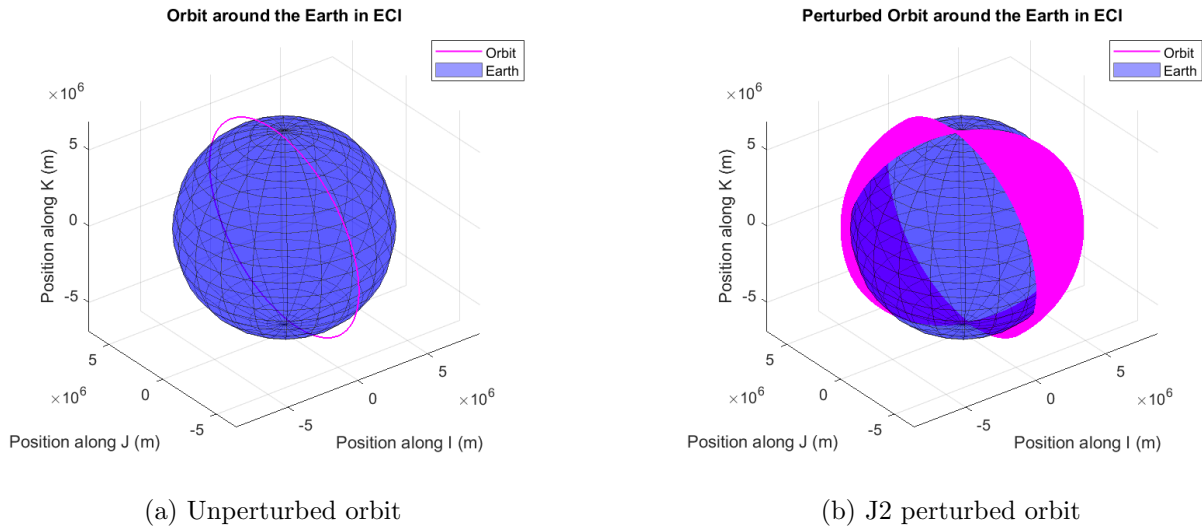


Figure 4: Simulated TDS orbital path starting on 15 June 2007 (1000 orbits).

1.2.d Unperturbed Numerical and Analytical Comparison

In the restricted two-body problem, the sole parameter varying with time is the mean anomaly M , which is related to the eccentric anomaly E by

$$M = \sqrt{\frac{\mu}{a^3}}(t - t_0) = E - e \sin E \quad (6)$$

The argument of latitude is related to the eccentric anomaly in the same way as the true anomaly for circular orbits

$$\tan \frac{E}{2} = \sqrt{\frac{1-e}{1+e}} \tan \frac{u}{2} \quad (7)$$

Using the same time steps as the numerical integration, Keplerian propagation was determined analytically by incrementing the mean anomaly, transforming mean anomaly into true anomaly, and applying the conic section equations (Eqs. 1 and 2) to resolve the position and velocity in the perifocal frame. With our previously validated code to transform orbital elements to the ECI frame, position and velocity were transformed from perifocal to ECI.

The position vector can be expressed in the Radial, Along-Track, and Cross-Track (RTN) frame by combining the rotation matrix R_{PQW}^{ECI} from Eq. 3 with a subsequent rotation by the argument of latitude:

$$R_{ECI}^{RTN} = R_{PQW}^{ECI} R_z(-u) \quad (8)$$

$$\vec{r}_{RTN} = R_{ECI}^{RTN} \vec{r}_{ECI} \quad (9)$$

Because the RTN frame is a non-inertial reference frame, the Theorem of Coriolis must be applied to express the velocity in RTN in addition to the coordinate transformation:

$${}^{ECI}\vec{v}_{ECI} = R_{RTN}^{ECI} \left[{}^{RTN}\vec{v}_{RTN} + \vec{\omega}_{ECI}^{RTN} \times \vec{r}_{RTN} \right] \quad (10)$$

$${}^{RTN}\vec{v}_{RTN} = (R_{RTN}^{ECI})^T {}^{ECI}\vec{v}_{ECI} - \vec{\omega}_{ECI}^{RTN} \times \vec{r}_{RTN} \quad (11)$$

where the angular velocity of the ECI frame with respect to the RTN frame as expressed in the ECI frame is simply the rate of change of the argument of latitude:

$$\vec{\omega}_{ECI}^{RTN} = [0, 0, \dot{u}]^T$$

Plotting the absolute error between the numerical and analytical solutions as shown in Figure 5, we can see that the position error grows to the order of millimeters and the velocity error grows to the order of micrometers per second after ten orbits. These results were obtained using a tolerance of 10^{-12} for the *ode45* solver and a step size of one-hundredth of the orbital period. As expected, increasing either of these two metrics led to an increase in error.

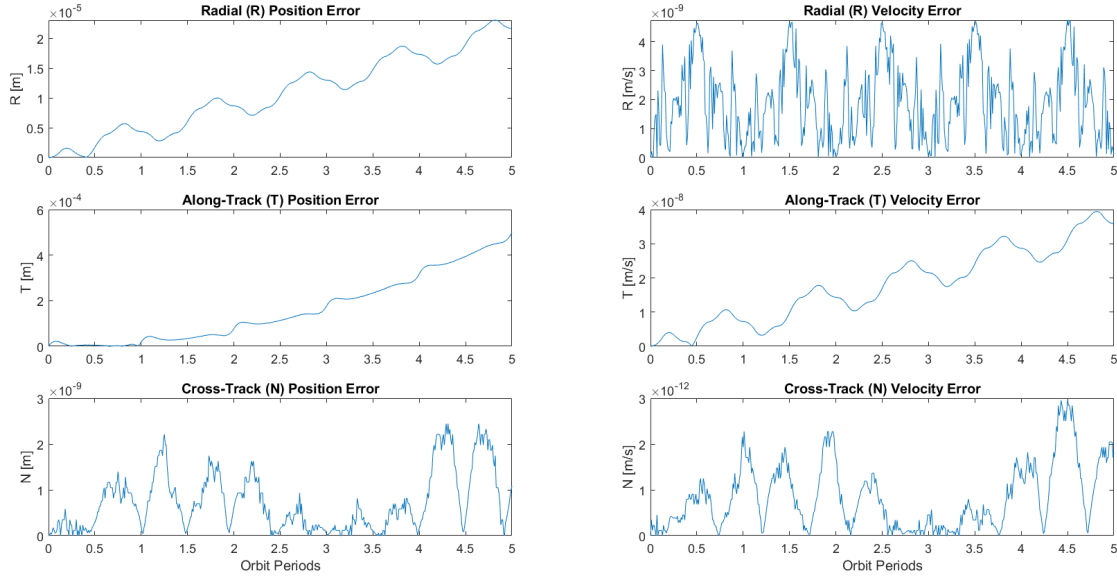


Figure 5: Absolute position and velocity errors of the numerical integration with respect to the analytical solution in the RTN frame.

1.2.e Osculating Orbital Elements from Numerical Simulation

Here we take the steps described in Vallado [6]. The implementation begins by constructing three vectors which define typical orbits (specific angular momentum \vec{h} , line of nodes \hat{n} , and line of apsides \hat{e}):

$${}^{ECI}\vec{h} = {}^{ECI}\vec{r} \times {}^{ECI}\vec{v} \quad (12)$$

$${}^{ECI}\hat{n} = \hat{K} \times {}^{ECI}\vec{h} \quad (13)$$

$${}^{ECI}\hat{e} = \frac{1}{\mu} \left[\left(\left\| {}^{ECI}\vec{v} \right\|^2 - \frac{\mu}{\left\| {}^{ECI}\vec{r} \right\|} \right) {}^{ECI}\vec{r} - \left({}^{ECI}\vec{r} \cdot {}^{ECI}\vec{v} \right) {}^{ECI}\vec{v} \right] \quad (14)$$

We can also compute the orbit shape (assuming non-parabolic) by the specific mechanical energy ϵ and semimajor axis a :

$$\epsilon = \frac{\left\| {}^{ECI}\vec{v} \right\|^2}{2} - \frac{\mu}{\left\| {}^{ECI}\vec{r} \right\|} \quad (15)$$

$$a = -\frac{\mu}{2\epsilon} \quad (16)$$

We finally find the orientation of the orbit:

$$i = \cos^{-1} \left(\frac{h_K}{\left\| {}^{ECI}\vec{h} \right\|} \right) \quad (17)$$

$$\Omega = \cos^{-1} \left(\frac{n_I}{\|ECI \hat{n}\|} \right) \quad (18)$$

$$u = \cos^{-1} \left(\frac{ECI \hat{n} \cdot ECI \vec{r}}{\|ECI \hat{n}\| \|ECI \vec{r}\|} \right) \quad (19)$$

In addition, checks in the code are performed to ensure that these angles are evaluated in the correct quadrants within the range $[0, 2\pi)$.

The orbital elements, specific angular momentum, and specific energy are plotted for simulations including and excluding J2 effects in Figure 6. For unperturbed orbit propagation, all orbital elements are constant except for the argument of latitude (u) as the satellite propagates its orbit. Additionally, the line of apsides defined by the vector e is constant while the specific angular momentum changes slightly in the \hat{K} component as shown in Figure 7. Over a period of 5 orbits, this variance was calculated to be on the order of $1m^2/s$, which is significantly smaller than the magnitude of specific angular momentum ($10^{10} m^2/s$). This discrepancy may be attributed to numerical integration errors.

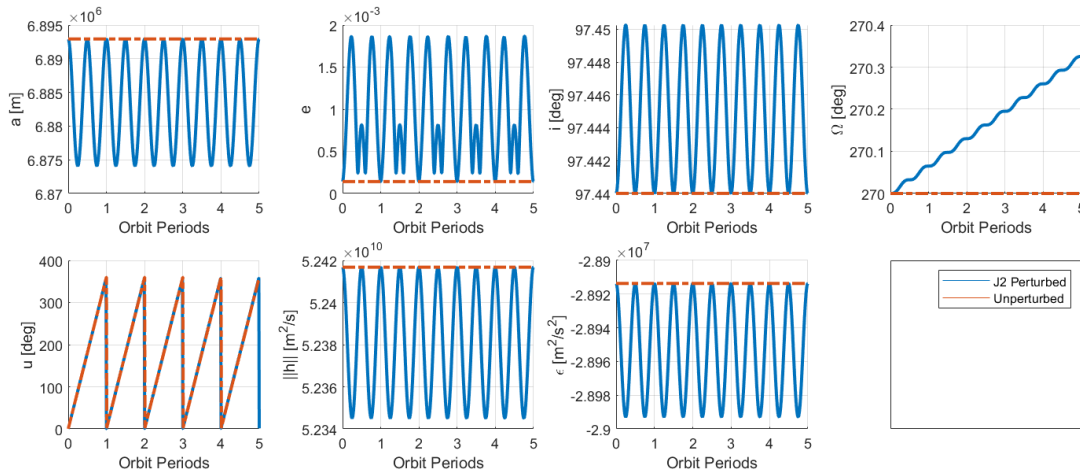


Figure 6: Orbital elements, specific angular momentum, and specific energy over 5 orbits for J2 (blue) and unperturbed (red) propagation.

Including J2 effects (short and long period oscillations), we find that all orbital elements, the specific mechanical energy, the line of apsides and the specific angular momentum exhibit periodicity. The right ascension of the ascending node Ω is clearly under secular effects as is expected for an inclined orbit due to precession. Likewise, we observe that the specific angular momentum demonstrates secular effects along the \hat{J} and \hat{K} directions, which is also to be expected due to the changes in RAAN.

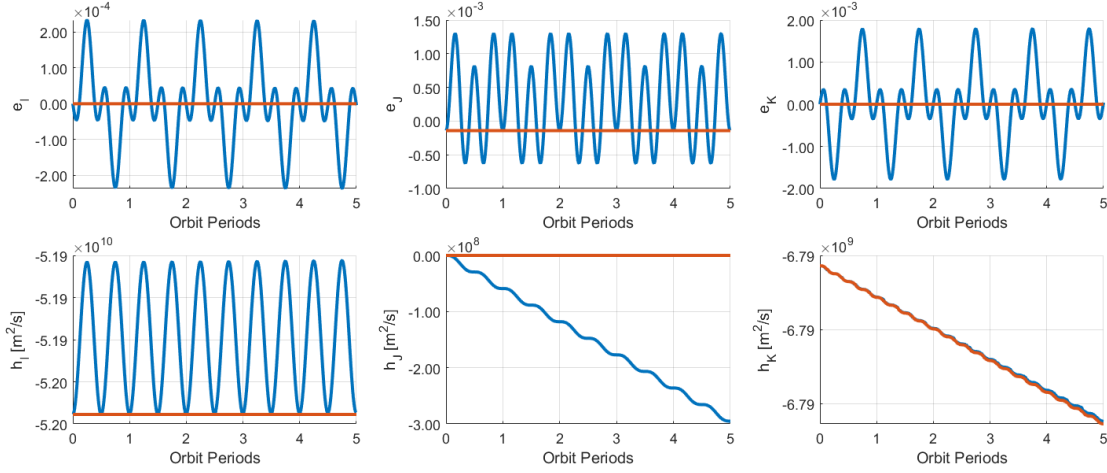


Figure 7: Line of apsides and specific angular momentum over 5 orbits for J2 (blue) and unperturbed (red) propagation.

1.2.f Mean Classical Orbital Elements

The differential equations for the mean classical orbital elements reflect zero variations in a , e , and i over time. The following linear differential equations are used in order to update the new state composed of orbital elements [7]:

$$\frac{d\Omega}{dt} = -\frac{3}{2}nJ_2 \left(\frac{R_E}{p}\right)^2 \cos(i) \quad (20)$$

$$\frac{du}{dt} = \frac{3}{4}nJ_2 \left(\frac{R_E}{a(1-(e_x^2 + e_y^2))}\right)^2 \left(\sqrt{1-(e_x^2 + e_y^2)}(3\cos^2 i - 1) + (5\cos^2 i - 1)\right) \quad (21)$$

$$\frac{de_x}{dt} = -\frac{3}{4}nJ_2 \left(\frac{R_E}{a(1-(e_x^2 + e_y^2))}\right)^2 e_y(5\cos^2 i - 1) \quad (22)$$

$$\frac{de_y}{dt} = \frac{3}{4}nJ_2 \left(\frac{R_E}{a(1-(e_x^2 + e_y^2))}\right)^2 e_x(5\cos^2 i - 1) \quad (23)$$

We follow a similar procedure as in the previous section to produce an evolution of the state vector across 5 orbits. Superimposing the resulting mean orbital elements, specific angular momentum, and specific energy with their osculating values in Figure 8 and Figure 9 shows they are generally in agreement.

Under averaging theory, we know the J2 perturbs the right ascension of the ascending node, the argument of periapsis and the mean anomaly. Since we are using the argument of latitude, the effects of the latter two get folded into this one. We see this clearly in Figure 8, where the only secular effects are observed in the right ascension of the ascending node. Although the argument of latitude appears to be unperturbed, taking a closer look at the region in Figure 10 shows that the values are slightly precessing. Note that this precession is due to J_2 , and that under the averaging theory we ignore motion that is periodic. This is why, unlike in the propagation of the position and velocity state vector, we do not see rapid changes in the argument of latitude as the satellites traverses its orbit.

Additionally, given the equations above, we not would expect a perfectly circular orbit to have any effects on its eccentricity by J_2 . In Figure 10, we do see very slight changes, and this is likely a numerical error.

When we calculate the initial eccentricity vector we arrive at a practically 0 value, but due to slight numerical error it is not exactly 0.

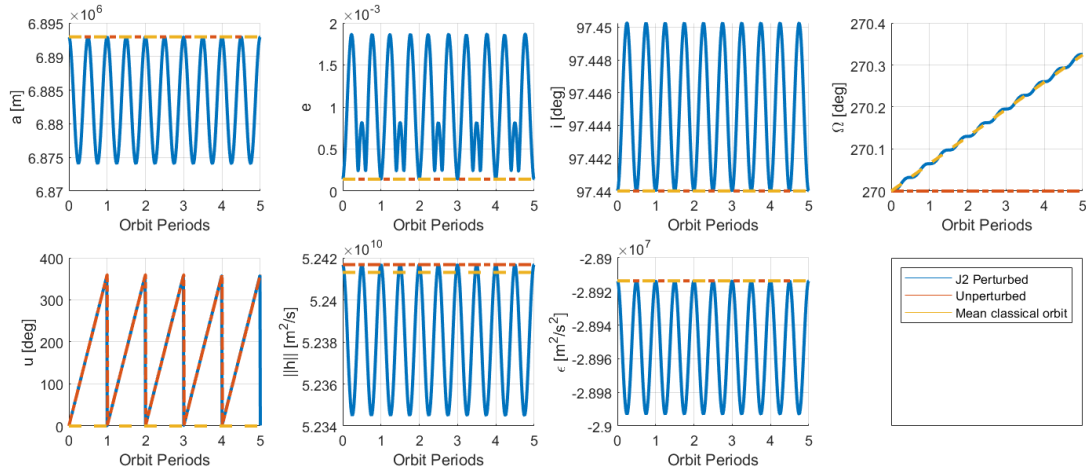


Figure 8: Orbital elements, specific angular momentum, and specific energy over 5 orbits for J2 (blue), unperturbed (red), and mean classical (yellow) orbit propagation.

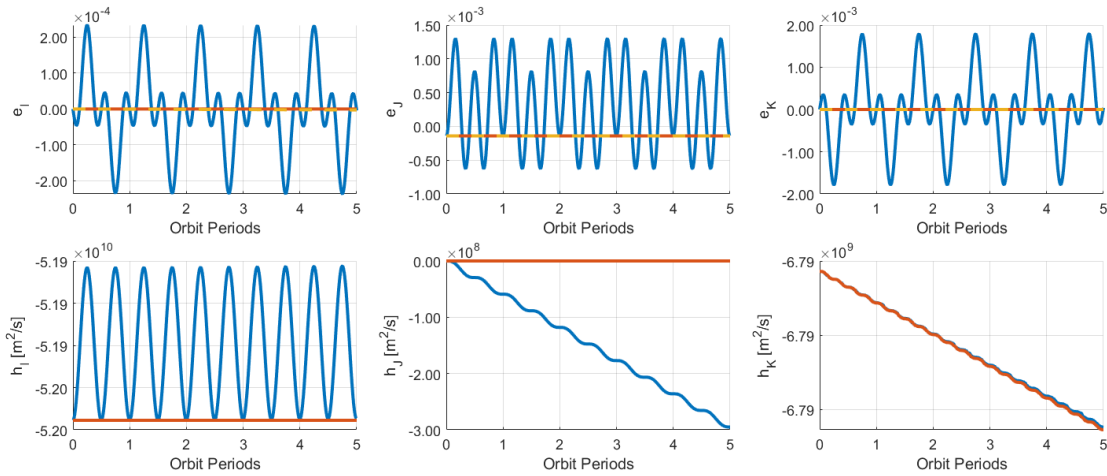


Figure 9: Line of apsides and specific angular momentum over 5 orbits for J2 (blue), unperturbed (red), and mean classical (yellow) orbit propagation.

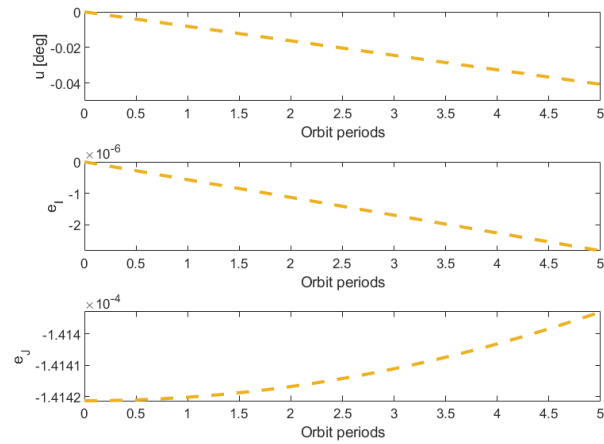


Figure 10: Isolating seemingly unperturbed parameters of the mean classical orbit propagation reveals small precession.

1.2.g Reconciling Osculating and Mean Orbital Elements

Inconsistencies during initialization can be mitigated using Brouwer theory to transform between mean and osculating values. We see this issue when comparing the unperturbed and the mean orbital elements of RAAN and argument of latitude u . Applying Brouwer theory would allow us to better match the behaviour of the mean classical orbit case in Figure 8 with the behaviour seen in the J2 perturbed case.

2 Problem Set 2

2.1 Problem 1: Everything is Relative

2.1.a Chief and Deputy Orbit Initialization

Non-singular orbit elements will be used since the TSX satellite flies in a circular orbit. TSX is selected as the chief orbit with TDX as its deputy. In this case, TDX employs e/i vector separation in order to have a safe orbit that avoids crossing paths with TSX. We will be modeling the first phase of the mission (preliminary DEM generation), reported with the following difference in eccentricity $a\delta e$, difference in inclination $a\delta i$, and difference in phase angle [8]:

$$a\delta e = 260 \text{ m}, \quad a\delta i = 222 \text{ m}, \quad \theta - \phi = 200^\circ$$

These offsets are transformed to the orbital elements used in this project using polar coordinates. The subscript 0 refers to the chief orbit and the subscript 1 refers to the deputy orbit.

$$\Delta e = \begin{bmatrix} \Delta e_x \\ \Delta e_y \end{bmatrix} = \delta e \begin{bmatrix} \cos(\phi) \\ \sin(\phi) \end{bmatrix} \quad (24)$$

$$\Delta i = \begin{bmatrix} \Delta i_x \\ \Delta i_y \end{bmatrix} = \delta i \begin{bmatrix} \cos(\theta) \\ \sin(\theta) \end{bmatrix} = \begin{bmatrix} i_1 - i_0 \\ (\Omega_1 - \Omega_0)\sin(i_0) \end{bmatrix} \quad (25)$$

Using these relations, the relative eccentricity and inclination of the chief and deputy may be determined. We design the phase angle $\theta = +45^\circ$, the argument of latitude in which the deputy crosses the orbital plane of the chief, in order to produce a safe relative orbit as will be shown. The initial conditions for this leader and follower setup are given in Table 3.

	a	e_x	e_y	i	Ω	u
TSX	6892.927 km	1×10^{-4}	1×10^{-4}	97.44°	270°	0°
TDX	6892.927 km	6.5814×10^{-5}	8.4059×10^{-5}	97.4413°	270.0013°	0°

Table 3: Initial orbital parameters of TSX and TDX in Helix formation.

2.1.b Numerical Integration of Relative Equations of Motion

Relative motion between the chief and deputy spacecraft can be derived as a 10-dimensional system of differential equations describing the relative acceleration of the deputy in the rotating RTN frame as $[\ddot{x}, \ddot{y}, \ddot{z}]$ and the acceleration of the chief as $[\ddot{r}_0, \ddot{\theta}]$. The system is represented by the state vector $[\vec{p}, \dot{\vec{p}}, r_0, \theta_0, \dot{r}_0, \dot{\theta}_0]$.

$$\ddot{x} - 2\dot{\theta}_0\dot{y} - \ddot{\theta}_0y - \dot{\theta}_0^2x = -\frac{\mu(r_0 + x)}{[(r_0 + x)^2 + y^2 + z^2]^{\frac{3}{2}}} + \frac{\mu}{r_0^2} \quad (26)$$

$$\ddot{y} + 2\dot{\theta}_0\dot{x} + \ddot{\theta}_0x - \dot{\theta}_0^2y = -\frac{\mu y}{[(r_0 + x)^2 + y^2 + z^2]^{\frac{3}{2}}} \quad (27)$$

$$\ddot{z} = -\frac{\mu z}{[(r_0 + x)^2 + y^2 + z^2]^{\frac{3}{2}}} \quad (28)$$

$$\ddot{r}_0 = r_0 \dot{\theta}_0^2 - \frac{\mu}{r_0^2} \quad (29)$$

$$\ddot{\theta}_0 = -\frac{2\dot{r}_0 \dot{\theta}_0}{r_0} \quad (30)$$

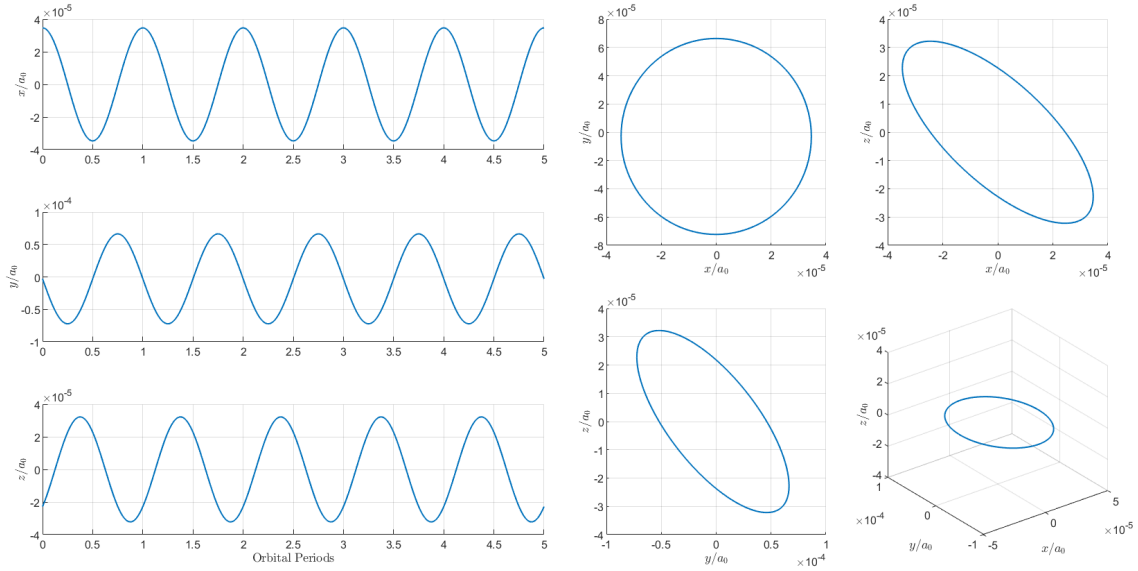


Figure 11: Numerically integrated relative RTN position of the deputy (TDX) with respect to the chief (TSX) using the non-linear equations of relative motion.

These differential equations are numerically integrated using *ode45*, and the results are shown in Figure 11 and 12. The corresponding initial conditions are found by finding the initial ECI position and velocities of the orbits from the orbital elements in part a. We then employ differences, coordinate transforms and the Theorem of Coriolis to find the correct initial conditions. The superscript 0 corresponds to the fact that these are initial conditions, while the subscript indicated the chief (0) or deputy (1). The rotation matrix and the corresponding rotation rates are taken with respect to the chief's orbit.

$$\theta_0 = u_0^0; \quad (31)$$

$$\dot{\theta}_0^0 = \sqrt{\frac{\mu}{a_0^3(1-e_0^2)^3}} \left(1 + e_0 \cos(\theta_0)\right)^2 \quad (32)$$

$${}^{ECI}\vec{\omega}^{RTN} = [0, 0, \dot{\theta}_0^0] \quad (33)$$

$$R_{ECI}^{RTN} = R_z(-\Omega_0)R_x(-i_0)R_z(-u_0^0) \quad (34)$$

$${}^{ECI}\vec{\rho}^0 = {}^{ECI}\vec{r}_1^0 - {}^{ECI}\vec{r}_0^0 \quad (35)$$

$${}^{ECI}\dot{\vec{\rho}}^0 = {}^{ECI}\vec{v}_1^0 - {}^{ECI}\vec{v}_0^0 \quad (36)$$

$${}^{RTN}\vec{\rho}^0 = R_{ECI}^{RTN} {}^{ECI}\vec{\rho}^0 \quad (37)$$

$${}^{RTN}\dot{\vec{\rho}}^0 = R_{ECI}^{RTN} {}^{ECI}\dot{\vec{\rho}}^0 - {}^{ECI}\vec{\omega}^{RTN} \times {}^{RTN}\vec{\rho}^0 \quad (38)$$

$${}^{RTN}\vec{r}_0^0 = R_{ECI}^{RTN} {}^{ECI}\vec{r}_0^0 \quad (39)$$

$$r_0^0 = \left\| {}^{RTN}\vec{r}_0^0 \right\|_2 \quad (40)$$

$$\dot{r}_0^0 = \left\| R_{ECI}^{RTN} {}^{ECI}\vec{v}_0^0 - {}^{ECI}\vec{\omega}^{RTN} \times {}^{RTN}\vec{r}_0^0 \right\|_2 \quad (41)$$

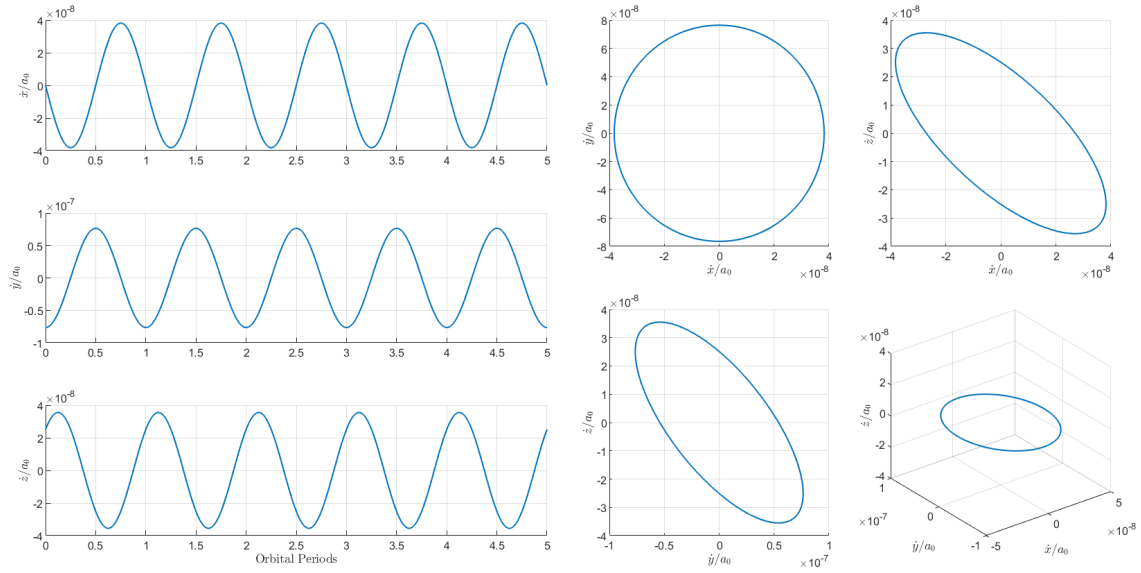


Figure 12: Numerically integrated relative RTN velocity using the non-linear equations of relative motion.

2.1.c Analytical Solution to Fundamental Orbital Differential Equations

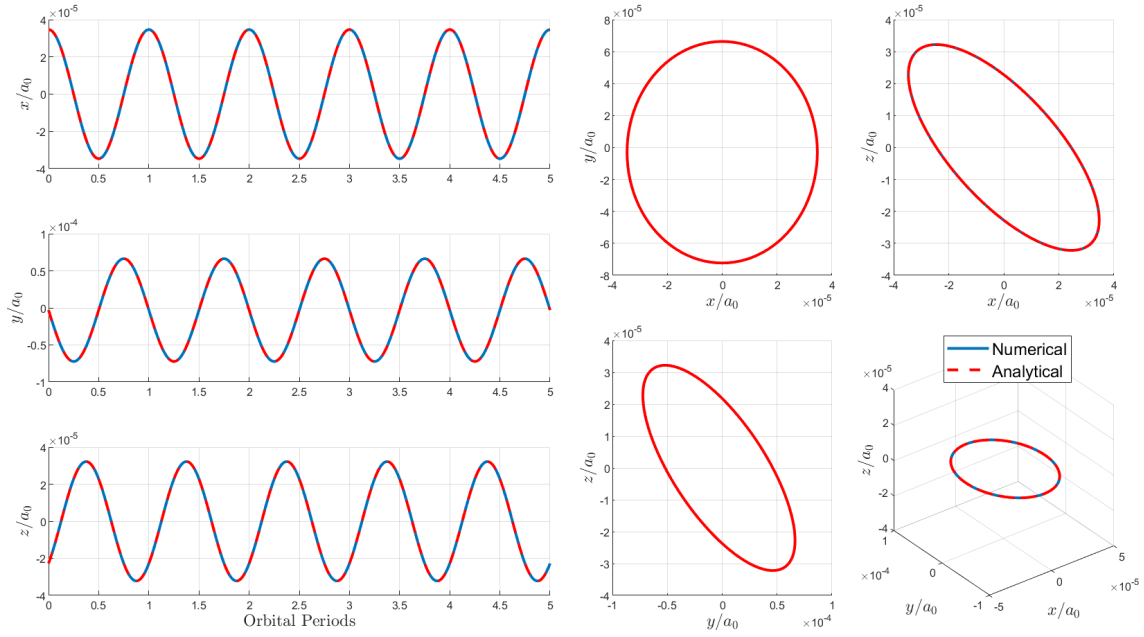


Figure 13: Overlaid numerically integrated (blue) and analytically determined (red) relative RTN position.

We choose to analytically solve for the absolute position of the chief and deputy using the fundamental orbital differential equations in order to adequately compare with the nonlinear relative equations of motion. We can then take the difference between the vectors in ECI, and perform a transformation from ECI to RTN as was done in 1.2.d. The resulting relative positions and velocities of the deputy with respect to the chief in the RTN frame is shown in Figure 13 and 14. Due to the fact that the numerical and analytical simulations show extremely small error, the position and velocity plots appear indistinguishable as they are stacked on top of one another as will be discussed in the next section.

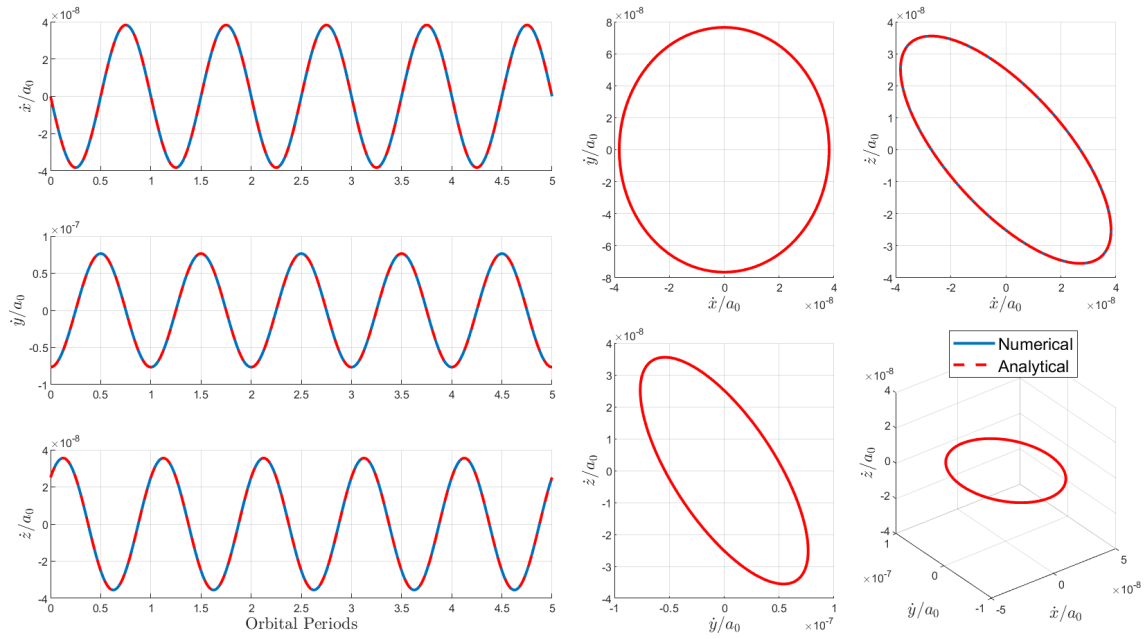


Figure 14: Overlaid numerically integrated (blue) and analytically determined (red) relative RTN velocity.

2.1.d Numerical and Analytical Comparison

The relative position as found by the analytical equations exhibits periodicity in the X, Y, and Z coordinates in the RTN frame and aligns closely with that found by the nonlinear numerical integration. Numerical error between the two approaches produces the largest difference on the order of picometers (10^{-12} meters) in the along-track direction as shown in Figure 15. The error in velocity is even smaller as be seen in Figure 16.

The error is similarly small for changing initial conditions when a 100-m difference is introduced in the semi-major axis. The order of magnitude in this case is also as large as 10^{-12} m as can be seen in Figure 17. However, as can be observed in Figure 18, this causes an along-track drift and the relative motion is no longer bounded.

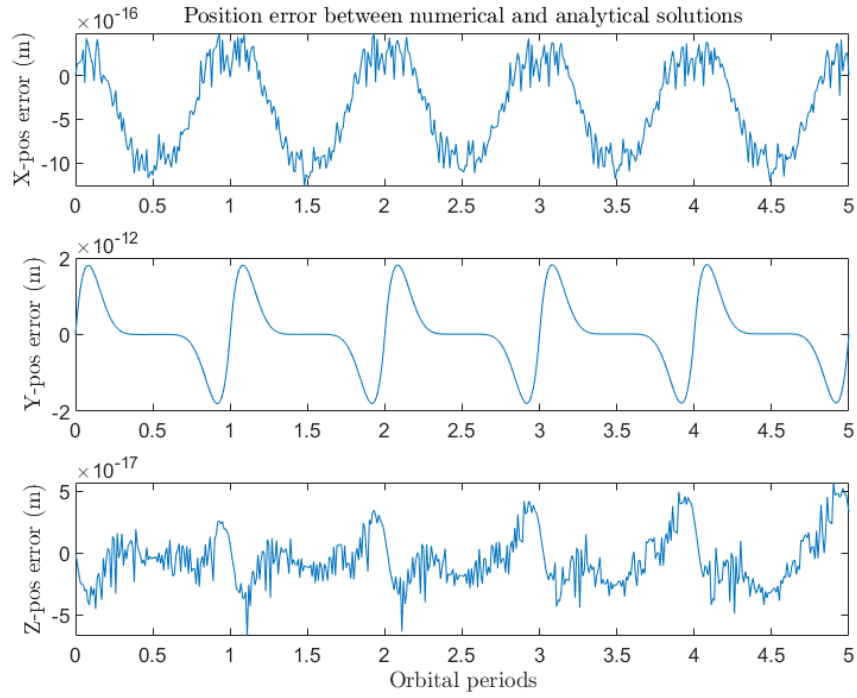


Figure 15: Position error in the RTN frame between the numerical and analytical solutions.

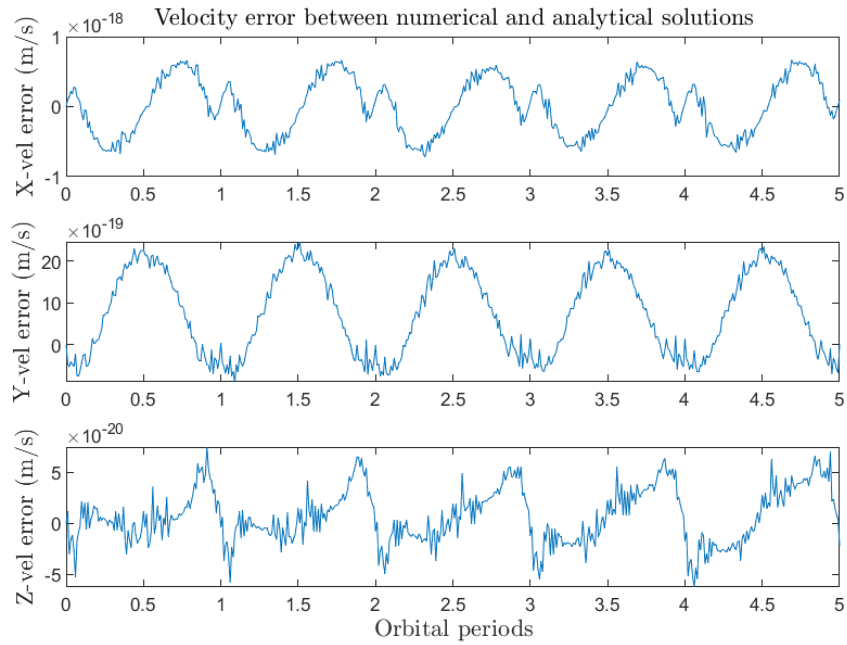


Figure 16: Velocity error in the RTN frame between the numerical and analytical solutions.

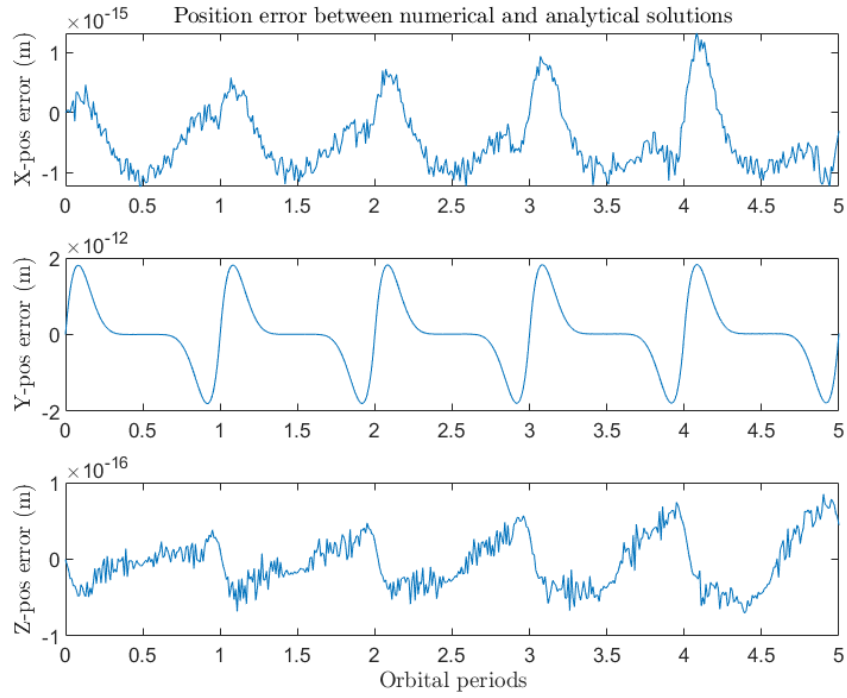


Figure 17: Position error between the numerical and analytical solutions with a difference in initial semi-major axis.

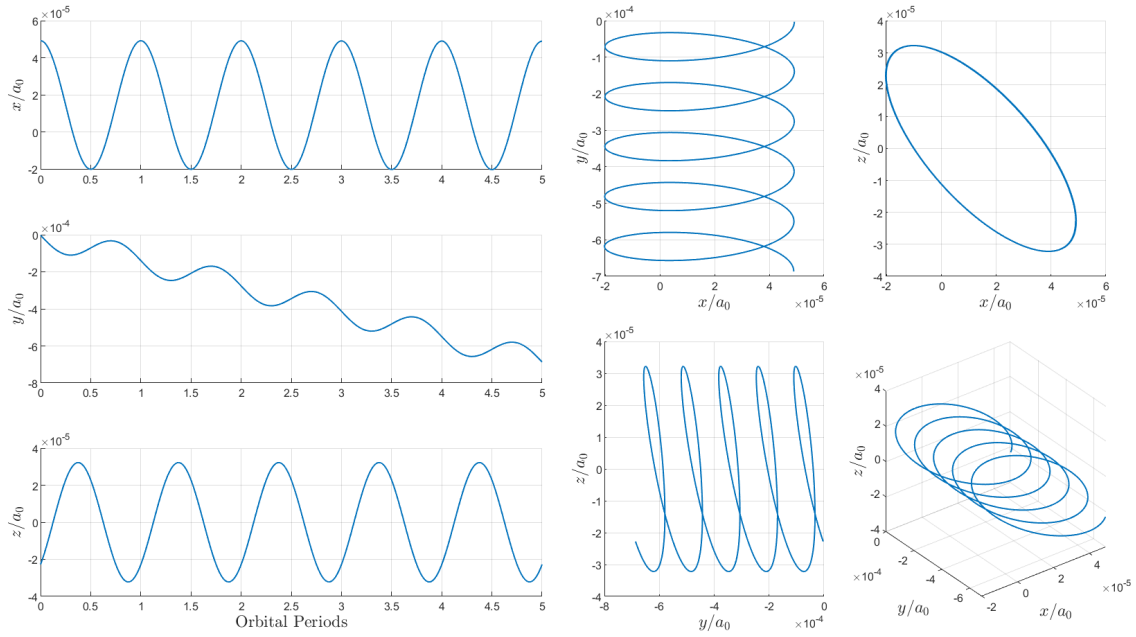


Figure 18: Numerically integrated relative RTN position with a difference in initial semi-major axis.

2.1.e Drift Correction Maneuver

To correct for the drift, an impulsive maneuver is executed to lower the semi-major axis by 100m and re-establish periodicity between the chief and deputy. Due to the Oberth effect, the location at which a maneuver will have the largest effect on the specific mechanical energy (and therefore require the lowest fuel) is the point of largest velocity magnitude. This occurs at the periapsis as is seen in the vis-viva equation. For perfectly circular orbits, the location of the maneuver is not as relevant since the velocity magnitude is constant – the Δv required does not significantly vary from one location to another. However, to be as precise as possible, we will implement this maneuver at the periapsis of the deputy's orbit since its orbit is slightly eccentric.

The required Δv of the maneuver can be calculated using the Gauss Variational Equations, expressed in the velocity frame in the following equations. Note that the velocity frame is equivalent to the RTN frame at periapsis.

$$\frac{da}{dt} = \frac{2a^2 v}{\mu} a_v \quad (42)$$

$$\Delta a = \frac{2a^2 v_p}{\mu} \Delta v_T \quad \rightarrow \quad \Delta v_T = \Delta a \frac{\mu}{2a^2 v_p} \quad (43)$$

$$v_p = \sqrt{\mu \left(\frac{2}{r_p} - \frac{1}{a} \right)}, \quad r_p = a(1 - e) \quad (44)$$

Therefore, we will have an impulsive maneuver at periapsis in the along-track direction of:

$$\Delta v_T = -0.0552 \text{ m/s}$$

2.1.f Maneuver Simulation

As shown in Figure 19, the applied Δv_T maneuver (which was applied to change only the semi-major axis) corrects the along-track drift and restores periodic relative motion between the two spacecraft.

Since the orbit simulation begins at the periapsis, after 3 orbits the Δv_T is applied. This is observed as a discontinuity in the along-track velocity component at the beginning of the fourth orbit as shown in Figure 20.

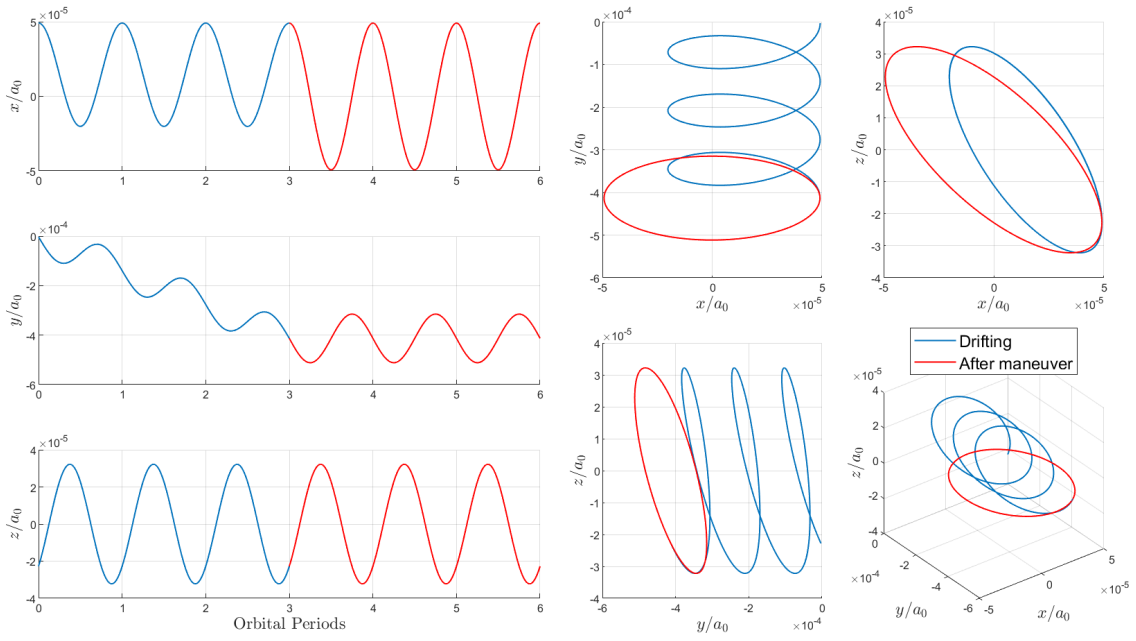


Figure 19: Numerically integrated relative RTN position before (blue) and after (red) the maneuver.

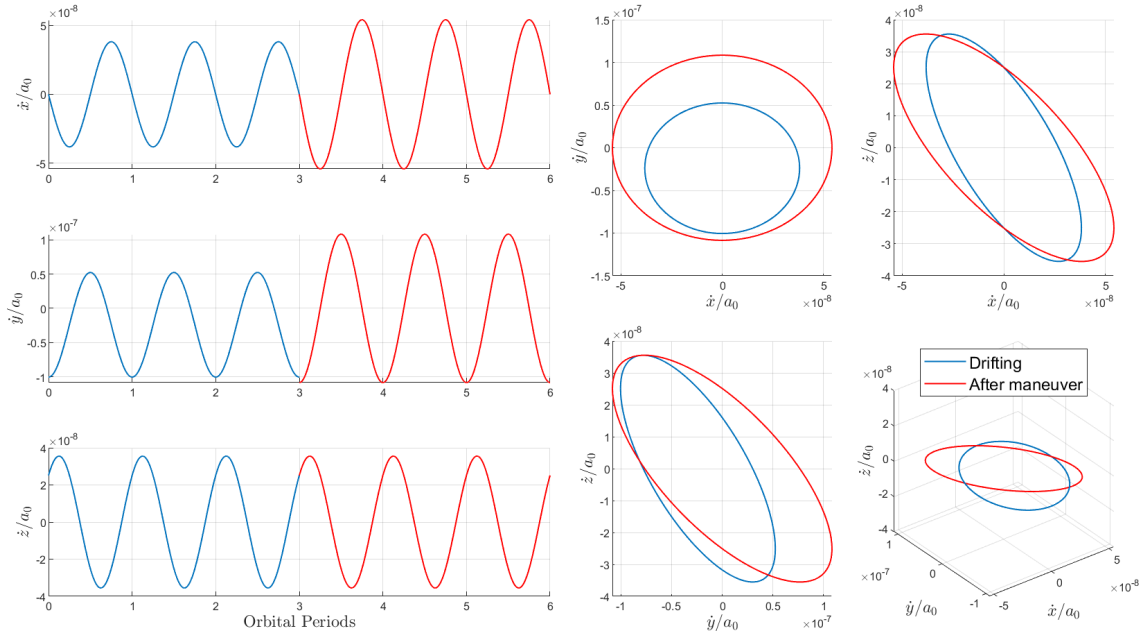


Figure 20: Numerically integrated relative RTN velocity before (blue) and after (red) the maneuver.

3 References

- [1] H. J. Kramer. “Tdx (tandem-x).” (Sep. 2016), [Online]. Available: <https://www.eoportal.org/satellite-missions/tandem-x>.
- [2] G. Krieger, A. Moreira, H. Fiedler, *et al.*, “TanDEM-x: A satellite formation for high-resolution SAR interferometry,” *IEEE Transactions on Geoscience and Remote Sensing*, vol. 45, no. 11, pp. 3317–3341, Nov. 2007, ISSN: 1558-0644. DOI: [10.1109/TGRS.2007.900693](https://doi.org/10.1109/TGRS.2007.900693).
- [3] H. J. Kramer. “Tsx (terrasar-x).” (Jun. 2012), [Online]. Available: <https://www.eoportal.org/satellite-missions/terrasar-x>.
- [4] A. I. Flores-Anderson, K. E. Herndon, R. B. Thapa, and E. Cherrington, *The Synthetic Aperture Radar (SAR) Handbook: Comprehensive Methodologies for Forest Monitoring and Biomass Estimation*. SERVIR Global Science Coordination Office, Apr. 2019. DOI: [10.25966/nr2c-s697](https://doi.org/10.25966/nr2c-s697).
- [5] R. R. Bate, D. D. Mueller, and J. E. White, *Fundamentals of astrodynamics*, en. New York: Dover Publications, 1971, ISBN: 978-0-486-60061-1.
- [6] D. A. Vallado, *Fundamentals of Astrodynamics and Applications*. 1997.
- [7] K. T. Alfriend, S. R. Vadali, P. Gurfil, J. P. How, and L. S. Breger, *Spacecraft Formation Flying: Dynamics, Control, and Navigation*. Elsevier Astrodynamics Series, 2010.
- [8] O. Montenbruck, R. Kahle, S. D’Amico, and J.-S. Ardaens, “Navigation and control of the TanDEM-x formation,” *The Journal of the Astronautical Sciences*, vol. 56, no. 3, pp. 341–357, Sep. 1, 2008, ISSN: 0021-9142. DOI: [10.1007/BF03256557](https://doi.org/10.1007/BF03256557). [Online]. Available: <https://doi.org/10.1007/BF03256557>.

4 Appendix A: Code

All code for this project can be found in the following [GitHub repository](#).